Molecular Detection for Unconcentrated Gas With ppm Sensitivity Using 220-to-320-GHz Dual-Frequency-Comb Spectrometer in CMOS

Cheng Wang, *Student Member, IEEE*, Bradford Perkins, Zihan Wang, and Ruonan Han, *Member, IEEE*

***Abstract*—Millimeter-wave/terahertz rotational spectroscopy of polar gaseous molecules provides a powerful tool for complicated gas mixture analysis. In this paper, a 220-to-320-GHz dual-frequency-comb spectrometer in 65-nm bulk CMOS is presented, along with a systematic analysis on fundamental issues of rotational spectrometer, including the impacts of various noise mechanisms, gas cell, molecular properties, detection sensitivity, etc. Our comb spectrometer, based on a high-parallelism architecture, probes gas sample with 20 comb lines simultaneously. It does not only improve the scanning speed by 20×, but also reduces the overall energy consumption to 90 mJ/point with 1 Hz bandwidth (or 0.5 s integration time). With its channelized 100-GHz scanning range and sub-kHz specificity, wide range of molecules can be detected. In the measurements, state-of-the-art total radiated power of 5.2 mW and single sideband noise figure of 14.6–19.5 dB are achieved, which further boost the scanning speed and sensitivity. Finally, spectroscopic measurements for carbonyl sulfide (OCS) and acetonitrile (CH_3CN) are presented. With a path length of 70 cm and 1 Hz bandwidth, the measured minimum detectable absorption coefficient reaches $\alpha_{gas,min} = 7.2 \times 10^{-7}$ cm^{-1}. For OCS that enables a minimum detectable concentration of 11 ppm. The predicted sensitivity for some other molecules reaches ppm level (e.g., 3 ppm for hydrogen cyanide), or 10 ppt level if gas preconcentration with a typical gain of 10^5 is used.**

***Index Terms*—CMOS, frequency comb, molecular spectroscopy, terahertz, transceiver.**

I. Introduction

ULTRA sensitive gas sensing is of great importance in environmental monitoring, industrial process control, hazardous agent detection, etc. [1]. It is also gaining increasing interests in clinical disease diagnosis. One important application is the molecular analysis of human exhaled breath [2], [3], which contains abundant volatile organic compounds (VOCs). Many of these VOCs, with concentrations ranging from *ppm* to *ppb* levels, have unique physiological basis [4], [5]. For example, hydrogen sulfide, acetone and toluene have strong correlation with halitosis, diabetes and lung cancer, respectively.

Current technologies for gas sensing includes: (1) gas chromatography/mass spectroscopy (GC/MS), which achieves *ppb* level sensitivity with pre-concentration techniques. However, it is ineffective for the identification of different compounds with similar mass spectra [5]; (2) selected-ion flow-tube mass spectroscopy (SIFT-MS) and proton transfer reaction-mass spectrometry (PTR-MS) , which detect ionized molecules produced by gas-phase collisions. They have *ppt* level sensitivity but the specificity is also limited; (3) mid-Infrared spectroscopy [6] detects the vibrational spectrum of gas molecules, which is sensitive due to the strong absorption intensity in infrared range. However, the limited tunability and linewidth of the light source make it less effective for complicated mixture analysis; (4) MEMS resonator based chemical sensors [7]–[9], which measure the variation of resonate frequency after absorption of gas molecules, have promising mass resolution but still suffer from selectivity issue; (5) electrochemical sensors, which is low cost but can only detect specific chemical species.

Rotation of polar gaseous molecules have quantized energy states in millimeter-wave and THz range. When molecules are excited by electromagnetic waves with photon energy matching that of the rotational state transitions, absorption spectral lines can be measured [10], [11]. The absorption intensity, as a result of degenerated quantum state number (increase with frequency) and probability for unoccupied quantum states (decrease with frequency), peaks at low-THz frequencies for most gaseous molecules. THz rotational spectroscopy is a powerful tool for gas sensing over the aforementioned technologies for the following reasons:

1) Simultaneous identification/analysis for a wide range of molecules is enabled through broadband scanning. Molecular spectral lines all follow a quasi-periodic pattern in frequency domain, and the "period" is determined by the dipole moment, weight, etc. of molecules. In fact, a spectroscopic bandwidth of 100 GHz allows the coverage of most of the chemical species under interest, including very light molecules such as hydrogen cyanide (HCN), which has a repetitive spectral line every 88.61 GHz [12].

Manuscript received January 23, 2018; accepted March 1, 2018. Date of publication April 5, 2018; date of current version June 5, 2018. This work was supported in part by the National Science Foundation (ECCS-1653100), in part by the Advanced Concepts Committee funding from MIT Lincoln Laboratories, TDK USA Corporation, and in part by MIT Center for Integrated Circuits and Systems. This paper was recommended by Associate Editor P. Mohseni. *(Corresponding author: Cheng Wang.)*

C. Wang, Z. Wang, and R. Han are with the Department of Electrical Engineering and Computer Science, Massachusetts Institute of Technology, Cambridge, MA 02139 USA (e-mail: wangch87@mit.edu; zihanw@mit.edu; ruonan@mit.edu).

B. Perkins is with MIT Lincoln Laboratory , Lexington, MA 02421-642 USA (e-mail: Bradford.Perkins@ll.mit.edu).

Color versions of one or more of the figures in this paper are available online at http://ieeexplore.ieee.org.

Digital Object Identifier 10.1109/TBCAS.2018.2812818

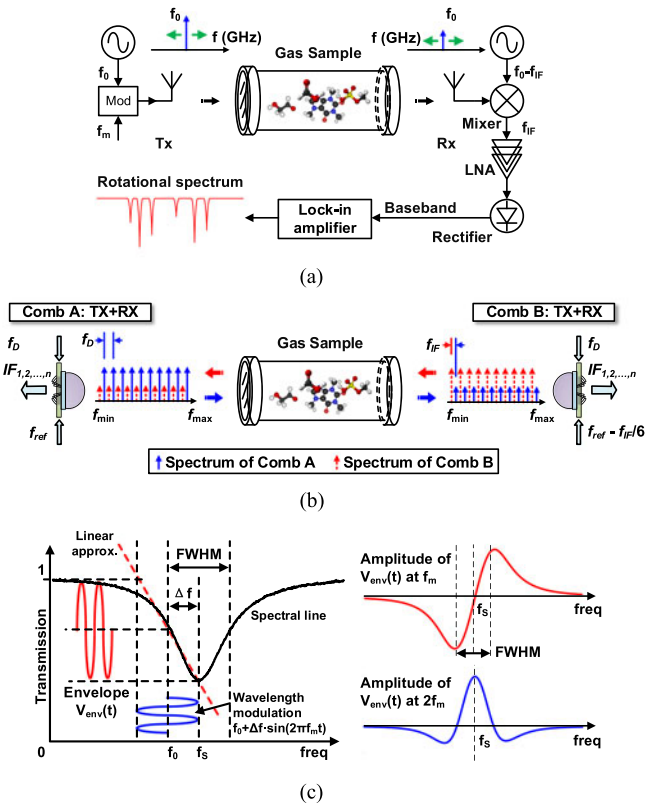

Fig. 1. (a) Conventional single-tone spectroscopy. (b) Dual-frequency-comb spectroscopy architecture. (c) Wavelength modulation spectroscopy (WMS).

2) The width of spectral lines in the Doppler-limited regime (at low pressure) is around 1 MHz. The corresponding spectral-line quality factor of Q $\sim 10^6$ leads to ultra-high detection specificity. Spectral overlap from different molecules is highly unlikely. The sub-kHz frequency resolution (at least 3 orders lower than the spectral line width) is also supported by nowadays THz electronics. Both of the narrow spectral lines and high quality THz signal sources make THz spectrometers capable of analyzing complex gas mixtures in details.
3) Previously, sensitive THz spectrometers using discrete compound III-V semiconductor components are reported. Working in conjunction with a widely adopted, industrial standard gas pre-concentration gain of 10^5, *ppt*-level sensitivity is achieved [13], which is comparable with state-of-the-art gas sensors.

Recently, rapid development of silicon-based THz integrated circuits brings about new opportunities for low-cost, energy-efficient rotational spectrometers at chip scale. As shown in Fig. 1(a), the spectrometer architecture widely adopted in prior arts performs molecular probing using a single tunable tone [14]–[17]. Although relatively compact and convenient to implement, it has several disadvantages: (1) the full-band scanning is time consuming. To scan a 100-GHz bandwidth with 10-kHz resolution and 1-ms integration time per point, it consumes $\sim$ 3 hours in total. (2) It suffers from power efficiency and sensitivity degradation due to the need for lossy tunable components and low Q-factor resonators to deliver broadband coverage. (3) As discussed in Section II-D, the maximum radiation power density for probing is set by the molecular saturation effect. As a result, an upper speed limit exists for this architecture due to the maximum achievable signal-to-noise ratio (SNR) per frequency step. Besides single-tone spectrometers, a 260 GHz pulse-based radiator with 24.7 GHz bandwidth for spectroscopy has been implemented [18]. However, due to the low duty cycle of pulse modulation, 80% of the RF energy is lost, which leads to low SNR. Without phase locking, it also lacks kHz-level tunability. Pulsed echo spectrometer [19] reduces the required RF power. But it needs to mechanically adjust resonant frequency of the cavity, which slows down the scanning speed. The reported frequency accuracy of its signal source is 0.1 ppm or 10 kHz. In [20], THz comb is generated through nonlinear optics using periodic laser pulses. This approach provides abundant comb lines from 100 GHz to 2 THz with frequency interval of 250 MHz. However, it comes with lower average radiated power and insufficient frequency resolution ($\sim$25 MHz).

In this paper, a 220-to-320 GHz, dual-frequency-comb spectrometer in 65-nm bulk CMOS process is presented. As shown in Fig. 1(b), the spectrometer probes the gas molecule sample using two counter-propagating comb signals rather than a single tunable tone. Each radiated comb signal has 10 continuous-wave, evenly-spaced frequency tones. Generation and heterodyne detection of the two comb signals are conducted simultaneously. The two comb spectra can also be shifted, so that a 100-GHz bandwidth is seamlessly covered. Through the parallel spectral scanning with the 20 comb lines, the scanning speed is enhanced by a factor of 20×. Since each comb line sweeps within only a small fractional bandwidth, peak efficiency is maintained, breaking the aforementioned bandwidth-efficiency trade-off in single-tone spectrometers. The measured silicon chip achieves state-of-the-art 5.2-mW radiated power and 14.6 $\sim$19.5 dB single sideband noise figure (SSB NF). To our best knowledge, these represent the highest power and sensitivity performance in THz silicon electronics.

The operation principles of the THz frontend circuits were originally presented in [21] and later described in details in [22]. In addition to including these contents (Section III) for completeness, this paper mainly focuses on the systematic analysis and design considerations of the work (in Section II), as well as extensive discussions and experiments for molecular sensing (in Section IV), which are not presented in [21] and [22]. In particular, the overall system performance is validated by measurements using OCS and acetonitrile gas samples, which give a minimum detectable absorption coefficient of $\alpha_{\text{gas,min}} = 7.2 \times 10^{-7}$ cm^{-1} with 1 Hz bandwidth. For OCS, our spectrometer reaches a minimum detectable concentration of 11 *ppm* and 0.1 *ppb* (if using standard gas pre-concentration with a gain of 10^5). Its sensitivity for some molecules with larger absorption (such as hydrogen cyanide (HCN)) should further reach a few *ppm* (without pre-concentration) and tens of *ppt* (with pre-concentration). Finally, conclusions, a comparison with other gas sensors in silicon, as well as perspectives for future work are given in Section V.

II. Performance Analysis of Spectroscopic System

Sensitive spectrometer design requires a comprehensive consideration for the on-chip electronics, molecular properties, gas cell, and their interactions. Systematic analysis and optimizations of these factors will be presented in this section. As is shown later in Section III, the generation and detection of each comb frequency tone are performed by a THz transceiver unit in each comb chip (Fig. 4). For each pair of comb tones, the circuit operation are the same as a typical single-tone heterodyne spectrometer shown in Fig. 1(a). In mmW/terahertz range, cascaded heterodyne receiver and square-law detector are preferable over direct square-law power detection due to its higher sensitivity. Normally, standing wave is formed inside the gas cell, which is due to multi-reflection between the inlet and outlet THz-signal windows. It introduces significant periodic RF power variation in frequency domain. The length of gas chamber is about λ/2 of the RF power variation frequency (70 cm gas cell for a variation frequency of 214 MHz). Thus, even if no spectral lines exist, the system has a baseline fluctuation. Wavelength modulation spectroscopy (WMS) [23] with a modulation frequency of f_m and a deviation frequency of Δf (illustrated in Fig. 1(c)) is adopted, which measures the derivatives of the overall transmission response. Since the derivatives (especially the 2nd-order derivative) of the baseline are much smaller than that of the spectral lines, this approach effectively reduces the impact from the baseline fluctuation. In addition, for maximum baseband response, Δf is chosen to be half of the full width at half maximum ($0.5 \times FWHM$) of the spectral line (for output at f_m) or $FWHM$ (for output at $2f_m$), respectively. Note that analyses throughout this section are based on single-channel circuits (Fig. 1(a)) and the above detection principles, but are also applicable to our comb spectrometer.

A. Impact of Receiver Noise on Sensitivity

In Fig. 1(a), the received signal power changes according to the gas absorption intensity, which can be expressed as:

$$\Delta P = P_0 e^{-\alpha_0 L}(1 - e^{-\alpha_{\rm gas} L}) \approx P_0 e^{-\alpha_0 L}\alpha_{\rm gas} L, \quad (1)$$

where P_0 is the transmitted signal power, $\alpha_{\rm gas}$ is the peak absorption coefficient at the center of spectral line, α_0 and L are the path loss coefficient and length of the gas cell. Here, we assume $\alpha_{\rm gas} L \ll 1$ given the normally low molecule concentration, and no extra loss exists besides path loss and gas absorption.

Next, the overall receiver noise is dominated by the input-referred noise temperature $T_n = T_0(F-1)$ of the mixer, where F is the mixer noise factor, and T_0 is the ambient temperature. Therefore, the RMS noise voltage referred at the receiver input side is $v_{n,RMS} = \sqrt{kT_n f_{ENBW} Z_0}$, where k is Boltzmann's constant, Z_0 is receiver input impedance and f_{ENBW} is the effective noise bandwidth. To investigate its impact on detection sensitivity, we note that the total voltage at the square-law detector input is:

$$V_{\rm in}(t) = [V_0 \sin(\omega_0 t) + v_n(t)] \cdot G_{\rm mixer}, \quad (2)$$

where V_0 is the amplitude of the receiver input voltage (and equals to $\sqrt{2Z_0 P_0 e^{-\alpha_0 L}}$ if no gas exists) and $G_{\rm mixer}$ is the mixer conversion gain. Meanwhile, the square-law detector is modeled as a polynomial function:

$$V_{\rm out}(t) = C_1 V_{\rm in}(t) + C_2 V_{\rm in}(t)^2 + C_3 V_{\rm in}(t)^3 + \cdots \quad (3)$$

As a result, the final baseband output of the square law detector is:

$$V_{\rm out} = C_2 G_{\rm mixer}^2 \left[\frac{V_0^2}{2} + 2V_0 \sin(\omega_0 t) v_n(t)|_{BB} + \cdots\right]. \quad (4)$$

The low-pass-filtered detector output signal is then:

$$V_{s,\rm out} = C_2 G_{\rm mixer}^2 \frac{V_0^2}{2}. \quad (5)$$

Within an output bandwidth of $\Delta\nu$ at baseband, the second term in (4) represents a down-conversion of both the upper and lower RF sideband noise v_n around ω_0 (i.e., $f_{ENBW} = 2\Delta\nu$). Therefore, in (3) the total integrated noise (RMS) at the detector output is:

$$V_{n,\rm out} = C_2 G_{\rm mixer}^2 V_0 \sqrt{2kT_n \Delta\nu Z_0}. \quad (6)$$

Equation (6) is also called Townes noise [10], which is dependent on the input signal power level. If assuming no gas absorption, the baseband SNR (in voltage) of the receiver, with a bandwidth of $\Delta\nu$, is then:

$$SNR_{BB}|_{v/v} = \frac{V_{s,\rm out}}{V_{n,\rm out}} = \frac{V_0^2}{2V_0\sqrt{2kT_n\Delta\nu Z_0}} = \frac{1}{2}\sqrt{\frac{P_0 e^{-\alpha_0 L}}{kT_n\Delta\nu}}, \quad (7)$$

A few conclusions are made out of the above derivations:

1) The ratio between the input RF signal power and the input-referred receiver noise with the same bandwidth of $\Delta\nu$ is:

$$SNR_{RF}|_{v/v} = \sqrt{\frac{P_0 e^{-\alpha_0 L}}{kT_n\Delta\nu}}. \quad (8)$$

By comparing (7) with (8), we see that an SNR degradation of 2× or 6 dB occurs. This, verified by our circuit simulation, is important for sensitivity estimation based on electronic RF performance and is later used in our experiments (Section IV).

2) Here, the shot noise of the detector is not included, but will ultimately limit the SNR even if the transmitter and receiver mixer are noise-free. Shot noise results from the charge injection over semiconductor barrier in the detector diode. Its current spectral density is $i_n^2 = 2q_e I_{DC}\Delta\nu$, where q_e is the charge of electron, and I_{DC} is the rectified DC output current. The associated ultimate SNR is therefore:

$$SNR_{BB,ShotNoise} = \sqrt{\frac{I_{DC}}{2q_e\Delta\nu}}. \quad (9)$$

Note that the current responsivity of a diode is ∼10 A/W, meaning that 0.1 mW of input power already leads to an $SNR_{BB,ShotNoise}$ of 5.6×10^7, or 160 dB with baseband bandwidth of $\Delta\nu = 1$ Hz. This is a few orders of magnitude larger than the SNR typically achieved by a THz frontend (see Section IV). Therefore, our THz spectrometer is not shot-noise limited.

3) In case of detection with modulation frequency f_m and frequency deviation $\Delta f = 0.5 \times FWHM$, the system researches maximum baseband SNR at f_m when the RF center frequency is $f_0 = f_s \pm 0.5 \times FWHM$, if a linear approximation rather than Lorentz or Gaussian profile is assumed, as shown in Fig. 1(c). The maximum baseband SNR is expressed as:

$$SNR_{BB}|_{v/v} = \frac{\Delta V_{s,\text{out}}}{V_{n,\text{out}}} = \frac{1}{2}\sqrt{\frac{P_0 e^{-\alpha_0 L}}{kT_n \Delta\nu}}(1 - e^{-\frac{\alpha_{\text{gas}} L}{2}}). \quad (10)$$

If $\alpha_{\text{gas}} L \ll 1$, (10) is simplified as:

$$SNR_{BB}|_{v/v} \approx \frac{1}{4}\sqrt{\frac{P_0 e^{-\alpha_0 L}}{kT_n \Delta\nu}}\alpha_{\text{gas}} L. \quad (11)$$

It indicates that when $\alpha_{\text{gas}} L \ll 1$ the molecule concentration (linearly proportional to α_{gas}) is linearity proportional to the input/output SNR *in voltage* rather than *in power*. That means, for example, even if the receiver noise figure is reduced by 20 dB, the sensitivity of the spectrometer (in terms of *ppx*) is only improved by 10×. This is later verified by our experiments in Fig. 12. In addition, it should also be noticed that due to the non-ideal profile of spectral lines, the expression of actual SNR differs slightly from (11). For instance, 2 dB SNR degradation is expected for a Lorentzian profile (pressure induced broadening), and 0.6 dB SNR degradation is expected for Gaussian profile (Doppler limited broadening). However, this error can be compensated by choosing a slightly larger Δf. Lastly, (11) can also be applied to the detection output at $2f_m$ with $\Delta f = FWHM$, where ∼3 dB lower SNR compared with WMS at f_m is obtained at the center frequency of spectral line (f_s, in Fig. 1(c)).

B. Impact of Transmitter Noise on Sensitivity

The amplitude and phase noise of the transmitter may also affect the sensitivity. To investigate this issue, we assume that the receiver is noiseless, and the IF signal, being a frequency-shifted version of the transmitted signal, is:

$$V_{\text{in}}(t) = [V_0 + a_n(t)]\cos[\omega_0 t + \phi_n(t)] \cdot G_{\text{mixer}}, \quad (12)$$

where V_0, $a_n(t)$, ω_0 and $\phi_n(t)$ are the signal amplitude, amplitude noise, carrier frequency and phase noise, respectively. The phase noise $\phi_n(t) = \phi_p \sin(2\pi f_m t)$ is assumed to have a sinusoidal form [24], where ϕ_p is the peak phase fluctuation, and $2\pi f_m$ is the offset frequency from ω_0.

First, if an input signal contains only phase noise ($a_n(t) = 0$), and the phase noise is assumed small, (12) is then written as:

$$\begin{aligned} V_{\text{in}}(t) &= V_0 \cos[\omega_0 t + \phi_p \sin(2\pi f_m t)] \cdot G_{\text{mixer}} \\ &\approx V_0 G_{\text{mixer}} \Big\{ \cos(\omega_0 t) - \frac{\phi_p}{2}[\cos(\omega_0 - 2\pi f_m)t \\ &\quad - \cos(\omega_0 + 2\pi f_m)t] \Big\} \end{aligned} \quad (13)$$

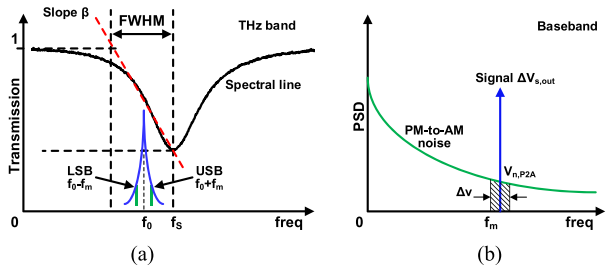

Fig. 2. (a) THz signal with two phase noise sidebands probes the spectral line and (b) The generated signal and PM-to-AM noise on the baseband.

The 2nd and 3rd items of (13) refer to the two phase noise sidebands (upper sideband (USB) and lower sideband (LSB) as shown in Fig. 2(a)). If no spectral lines exist at the probing frequency, the amplitudes of two sidebands are equal. After the square-law detection, the two sideband signals will cancel each other. As a result, the detector output voltage after low-pass filtering of (3) is:

$$V_{\text{out}} \approx \frac{1}{2}C_2 G_{\text{mixer}}^2 V_0^2 + C_1 V_{\text{in}}|_{LPF} + \cdots, \quad (14)$$

where the 1st term is the desired output. The 2nd term is the direct low-pass-filtered component of V_{in}, which includes the phase noise of V_{in} at offset larger than $\omega_0 - 2\pi\Delta\nu$. Typically, at 1-MHz offset frequency, the phase noise of THz signal is -80 dBc/Hz for oscillator-based sources and -100 dBc/Hz for multiplier-based sources. Therefore, the IF frequency should be sufficiently high, so that the close-in phase noise does not directly fall into baseband.

If the THz signal touches the spectral line, as shown in Fig. 2(a), PM-to-AM noise is generated. Because the slope of absorption coefficient on the edge of spectral line profile introduces amplitude imbalance on the two phase noise sidebands of (13). After square-law detection, the phase noise of THz signal is then down-converted into amplitude noise in the baseband due to imperfect sideband cancellation. If a linear approximation is assumed for the spectral line profile, and $\alpha_{\text{gas}} \ll 1$, the baseband signal at f_m is expressed as:

$$\Delta V_{s,\text{out}} \approx C_2 G_{\text{mixer}}^2 \frac{V_0^2}{2} FWHM \cdot \beta \cdot L, \quad (15)$$

where $\beta = \alpha_{\text{gas}}/FWHM$ is the slope of line profile. Since $\Delta V_{s,\text{out}}$ is located at f_m of baseband, only the phase noise close to frequency offset f_m matters, as shown in Fig. 2(b). Based on (3) and (13), the PM-to-AM noise at f_m of baseband is then expressed as:

$$V_{n,P2A} \approx C_2 G_{\text{mixer}}^2 V_0^2 \frac{\phi_P}{4} f_m \cdot \beta \cdot L. \quad (16)$$

The SNR in voltage due to PM-to-AM noise can then be calculated using the following equation:

$$SNR_{P2A}|_{v/v} \approx \frac{FWHM}{f_m \sqrt{\int_{f_m - \Delta\nu/2}^{f_m + \Delta\nu/2} PN_{SSB}(\nu) d\nu}}, \quad (17)$$

where $PN_{SSB}(\nu)$ is the single sideband phase noise of THz signal at frequency offset ν, and $\Delta\nu$ is integration bandwidth. Thus, for one spectral line with $FWHM$ of 1 MHz, f_m of

50 kHz and $\Delta\nu$ of 1 Hz, the phase noise at 50 kHz frequency offset needs to be at least -54 dBc/Hz for SNR of 10^4. But since $V_{n,P2A}$ decreases linearly with molecule concentration (i.e., smaller β), PM-to-AM noise only matters under high SNR. It is not a limiting factor for sensitivity, which is defined when SNR $= 1$.

Next, if the input contains only amplitude noise (i.e., $\phi_n(t) = 0$), it is similar to the input referred noise of receiver as shown in (4):

$$V_{\text{out}} \approx C_2 G_{\text{mixer}}^2 \left(\frac{V_0^2}{2} + V_0 a_n(t) + \frac{a_n(t)^2}{2} \right) + \cdots \quad (18)$$

We note that Townes noise in the 2nd term is again the dominant noise contributor, which results from the close-in amplitude noise of the transmitter signal. Fortunately, many mmW/terahertz CMOS sources (including ours) are based on heavily-driven nonlinear devices. The voltage swing of these devices is normally saturated or clipped by the power supply rail, which in turn suppresses the amplitude fluctuation caused by device noise. In addition, the power supply noise can potentially modulate the gain of transceiver and introduce amplitude noise to the baseband, and should therefore be maximally suppressed in the design of the entire system. Currently the noise of the receiver still dominates the overall SNR. In the future, however, when THz amplifier (with no squeezing of amplitude noise) becomes available, this issue should be revisited.

C. Spectral Broadening and Effect of Gas Cell Size

Both the inter-molecular collision (i.e., pressure) and the Doppler effect of Brownian motion cause spectral broadening. To achieve absolute specificity, gas pressure should be sufficiently low, so that the linewidth is only limited by Doppler effect, in order to avoid spectral-line overlap. It is noteworthy that optimum pressure increases with frequency [10], and in mmW/terahertz range, such pressure threshold is $\sim$10 Pa. In addition, when encapsulated inside a gas cell, molecules also have collisions with the sidewalls of gas cell, leading to additional broadening. Fortunately, this is not a predominant concern for THz spectrometer. Note that a spectral-line absorption $\gamma(f)$ due to collision follows a Lorenzian profile [25]:

$$\gamma(f) \propto \frac{1/2\pi\tau}{(f - f_0)^2 + (1/2\pi\tau)^2}, \quad (19)$$

where f_0 is resonance frequency and τ is the mean free time between molecular collisions. The full width of half maximum (FWHM) of the spectral line is therefore $\sim\frac{1}{\pi\tau}$. At the Doppler-limited pressure level ($\sim$10 Pa), the value of τ is $\sim$0.3 μs (hence a FWHM of $\sim$1 MHz), and the mean free path of molecules, determined by molecular diameter d and gas pressure P is:

$$\lambda_0 = \frac{kT_0}{\sqrt{2}\pi d^2 P}. \quad (20)$$

As an example, the mean free path for OCS ($d = 8$ $\mathring{A}$) is 140 μm. Even if a WR-3.4 waveguide (aperture size of 860 $\times$ 430 μm^2) is adopted as gas cell, which enables propagation of a 220–320-GHz TE_{01} wave, its dimension is still a few times larger than the above mean free path, and does not cause significant spectral broadening. In fact, the gas cell in our setup is even $\sim 100\times$ wider. Hence, the detection specificity is not degraded.

D. Molecular Saturation and Maximum Allowable Signal Power

High incident signal power may deplete the population of unexcited molecules, preventing additional photon absorption if the signal power is further increased. Such saturation effect, occurring at the tip of the spectral line first, not only leads to spectral broadening, but also nonlinear dependency between power absorption and gas concentration. The maximum probing signal power flux I can be estimated by [10]:

$$I = \frac{3\epsilon_0 c h^2 (\Delta f)^2}{D^2}, \quad (21)$$

where ϵ_0 is the permittivity of vacuum (8.85×10^{-12} F/m), c is the speed of light (3×10^8 m/s), h is Planck's constant (6.6×10^{-34} J·s), D is molecular dipole moment, and Δf is the absorption linewidth. The dipole moment of most polar molecules is on the order of 10^{-18} esu (in CGS system) or 3.3×10^{-30} C·m. Hence, the saturation power flux of a low-THz spectrometer is $\sim$0.3 mW/mm^2. Normally, the gas cell cross-sectional area is large enough that power saturation is avoided; however, if a single-mode WR-3.4 waveguide is used for sensor miniaturization, the maximum allowable signal power reduces to $\sim$0.1 mW, which is achievable in CMOS circuits (including our chip). This poses a *fundamental limit* for the SNR (shown in (11)) that a single-tone spectrometer can provide. In Section III-C, we will show how this problem is addressed by our comb spectrometer.

E. Optimum Path Length of Gas Cell and Maximum Achievable Sensitivity

The minimum detectable gas absorption coefficient $\alpha_{\text{gas,min}}$ is derived when the spectrometer baseband SNR (shown in (11)) is unity:

$$\alpha_{\text{gas,min}} = \frac{4}{L}\sqrt{\frac{kT_n\Delta\nu}{P_0 e^{-\alpha_0 L}}}. \quad (22)$$

A longer gas cell path length L enables stronger absorption but also higher waveguide power loss. In (22), an optimum length L_{opt} exists to achieve the minimal value of $\alpha_{\text{gas,min}}$. By having $\frac{d\alpha_{\text{gas,min}}(L)}{dL} = 0$, we derive:

$$L_{opt} = \frac{2}{\alpha_0}, \quad (23)$$

and the ultimate $\alpha_{\text{gas,min}}$ *achievable* by the electronics is:

$$\alpha_{\text{gas,min}} = 2e\alpha_0\sqrt{\frac{kT_n\Delta\nu}{P_0}}. \quad (24)$$

Therefore, the minimum detectable gas concentration is expressed as:

$$\gamma_{\min} = \frac{\alpha_{\text{gas,min}}}{\alpha_{\text{gas,pure}}} = \frac{2e\alpha_0}{\alpha_{\text{gas,pure}}}\sqrt{\frac{kT_n\Delta\nu}{P_0}}, \quad (25)$$

where $\alpha_{\text{gas,pure}}$ is the absorption coefficient of pure gas sample.

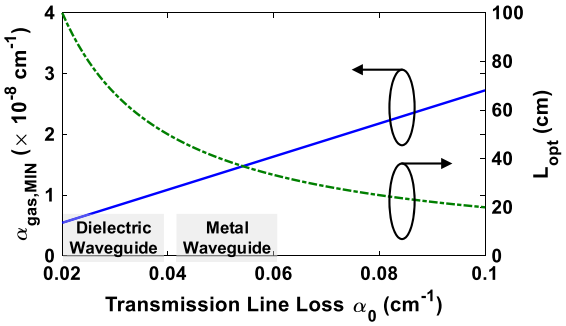

Fig. 3. Minimum detectable absorption coefficient $\alpha_{\text{gas,min}}$ and optimum length of gas cell L_{opt} and for spectrometers with different waveguide loss.

TABLE I
DETECTION SENSITIVITY OF VARIOUS GASES

Gas	Line Freq.[1] (GHz)	Absorption Intensity[2] (cm^{-1})	Detection Sensitivity (×ppm)
carbonyl sulfide (OCS)	292.04	0.048 @ 13 Pa	0.3
dinitrogen monoxide (N_2O)	301.65	6.3×10^{-3} @ 27 Pa	2.5
carbon monoxide (CO)	228.60	2.3×10^{-3} @ 40 Pa	6.8
nitric oxide (NO)	250.62	1×10^{-3} @ 40 Pa	16
sulfur dioxide (SO_2)	283.68	0.012 @ 4 Pa	1.3
nitrogen dioxide (NO_2)	256.16	7×10^{-4} @ 13 Pa	22
formaldehyde (H_2CO)	301.04	0.047 @ 4 Pa	0.2
hydrogen cyanide (HCN)	266.07	0.2 @ 2 Pa	0.08
methanol (CH_3OH)	318.54	5×10^{-3} @ 4 Pa	3.1

[1]Listed molecules normally have more than one spectral lines in the 220–320-GHz range. Only one line with high absorption intensity is selected here.
[2]Different molecules have different optimum detection pressure. The absorption intensity and detection sensitivity here are determined at the optimum pressure of each gas.
[3]Integration bandwidth $\Delta\nu = 1$ Hz, $T_0 = 296$ K, no pre-concentration techniques is assumed.

Currently, most THz spectrometers are based on the propagation of a collimated Gaussian beam inside a bulky gas cell. In the future, if single-mode metal rectangular waveguide is adopted as gas chamber, the optimum gas cell length L_{opt} and the associated minimum detectable absorption intensity $\alpha_{\text{gas,min}}$, as a function of path loss α_0, are plotted in Fig. 3. Here, a signal power of 0.1 mW is assumed, which is the threshold power for molecular saturation (Section II-D). A single sideband noise figure (NF) of 17 dB is assumed. Both metrics are achieved by our CMOS comb spectrometer (see Section IV). For a typical waveguide loss of 0.25 dB/cm (i.e., $\alpha_0 = 0.058$ cm^{-1}), the minimum detectable absorption intensity $\alpha_{\text{gas,min}}$ is 1.6×10^{-8} cm^{-1} with 1 Hz bandwidth at 296 K. The optimum gas cell length is ~35 cm. Table I shows the sensitivity or minimum detectable gas concentration based on the calculated minimum detectable absorption coefficient. A sensitivity at *ppm* level is predicted. A standard pre-concentration gain of 10^5 (like the one used in [13]) will further increase the spectrometer sensitivity to *ppt* level. According to Fig. 3, if low-loss hollow dielectric waveguide is used, the sensitivity can be further improved by 2 ~3×. Although the gas cell waveguide has an optimum length of 0.1 ~1 m, they can be folded to shrink the size of the spectroscopy system (in conjunction with the usage of micro vacuum pumps).

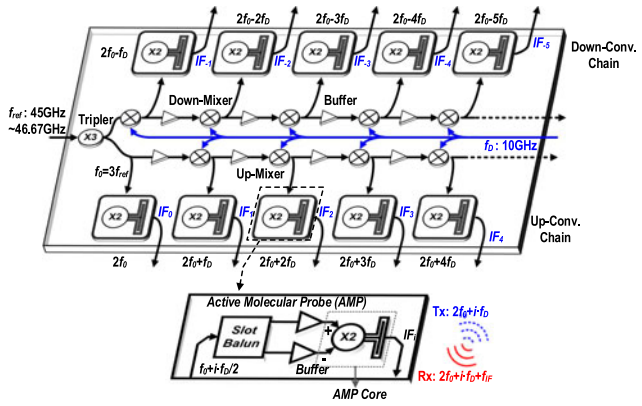

Fig. 4. Chip architecture of the frequency-comb-based spectrometer.

III. COMB-BASED SPECTROSCOPY: DESIGN AND CHIP-SCALE PROTOTYPE

In this section, we present the design of a new spectrometer, which leverages the large integration capability of CMOS technology, in order to improve spectral-scanning speed and sensitivity using parallelism.

A. Dual-Frequency-Comb, Bi-Directional Spectrometer

The dual-frequency-comb spectrometer consists of two identical frequency-comb chips. Each chip works under transmitting (TX) and receiving (RX) modes simultaneously. Shown in Fig. 1(b), 10 equally-spaced comb lines with 10 GHz frequency interval are transmitted from Chip A through the gas sample and coupled into Chip B via on-chip antennas. Meanwhile, inside Chip A, the above 10 comb lines are also used as local-oscillator (LO) signals for the heterodyne mixing of another 10 comb lines radiated from Chip B. A 950-MHz frequency offset is also created between the output radiation spectra of Chip A and Chip B as intermediate frequency ($f_{IF} = 950$ MHz).

Fig. 4 shows the block diagram of the comb chip [21]. The chip is driven by an external Q-band signals (f_{ref}) at ~46 GHz, which is then frequency multiplied by 3×. The frequency tripled signal at $3f_{\text{ref}}$ is injected into up- and down-conversion chains. The two chains produce evenly-spaced signal tones through cascaded single-sideband (SSB) mixers. Each SSB mixer shifts the frequency of single tone by 5 GHz; such frequency spacing is determined by a static digital frequency divider (÷2), which is built inside each mixer and has a 10 GHz clock input f_D. In simulation, the rejection of fundamental, image and inter-modulation components of the mixer is above 30 dB; the mixer conversion loss is 2.3 dB, which is compensated by inter-stage buffer amplifiers. Lastly, each mixer output is then frequency doubled and radiated through an "Active Molecular Probe (AMP)," which is further described next. In summary, a comb spectrum spanning from 220 to 320 GHz and with frequency spacing of 10 GHz is realized.

It is also noteworthy that, to fully cover the 100-GHz bandwidth, the comb spectrum only needs to shift by 10 GHz. In Fig. 4, this is readily accomplished by tuning the Q-band

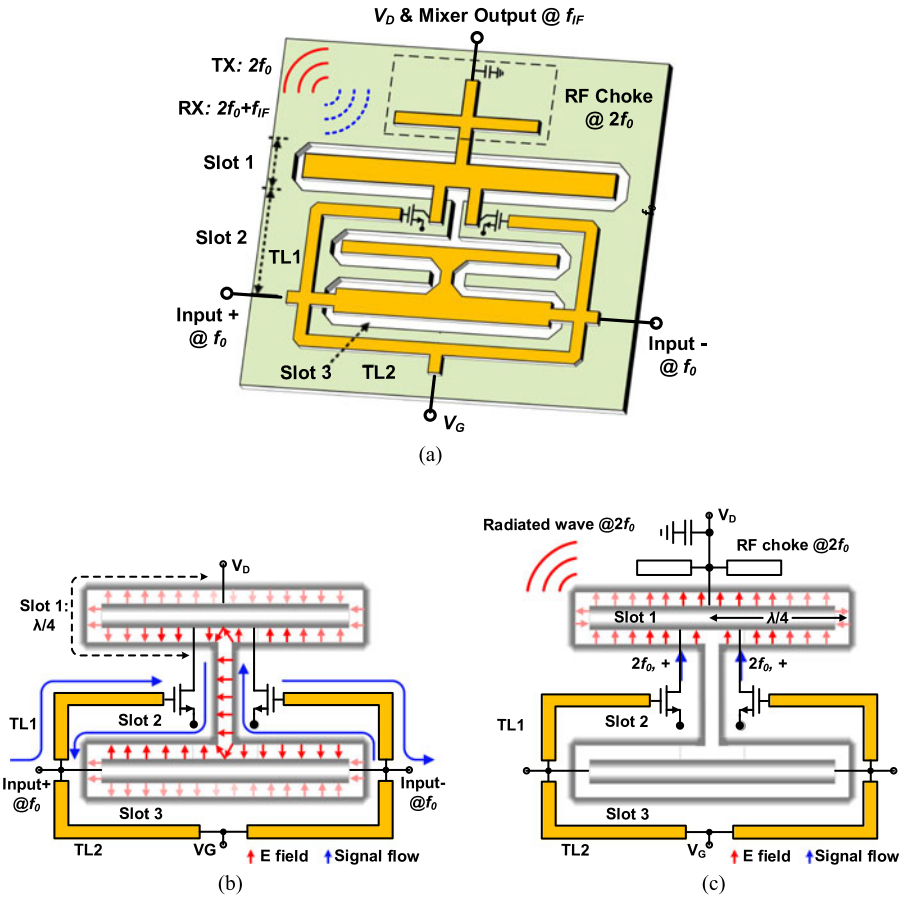

Fig. 5. Active Molecular Probe (AMP): (a) 3D circuit structure, (b) slot line based feedback for gain enhancement at f_0 and (c) harmonic isolation and radiation at $2f_0$.

driving signal $f_{\rm ref}$ from 45 to 46.67 GHz. On top of this, $f_{\rm ref}$ is wavelength modulated with a modulation frequency of f_m and frequency deviation of $\Delta f/6$, which is needed for molecular-sensing (illustrated in Fig. 1(c)).

B. Design of the Active Molecular Probe

The active molecular probe (AMP) inside each comb stage is the enabling circuit for simultaneous frequency-doubling and radiation of a transmitted comb line, as well as the down-mixing of another received comb line. The 3D structure of AMP is shown in Fig. 5(a), which consists of only one pair of MOSFETs.

For the frequency doubling of the TX mode, the MOSFETs are driven by a differential fundamental (f_0) signal through microstrip transmission line TL1 (Fig. 5(b)). Meanwhile, a signal feedback through Slot2 is deployed between the transistor drains and AMP inputs, so that the power gain of the transistor pair at f_0 is boosted to a theoretical limit of $\sim 4U$ [26], where U is the unilateral gain.[1] As one example, when f_0 equals 137.5 GHz, the gain is improved from 7 dB to 12 dB, which enhances the doubler efficiency from 18% to 43% [21]. The high efficiency is also due to the quarter-wavelength Slot1, which translates the virtual ground at the AMP top to high impedance termination at transistor drains. This generates large drain voltage swing, hence stronger nonlinearity.

At f_0, Slot2 supports the feedback flow of the input differential signal, because its cutoff frequency for the associated quasi-TE mode wave (Fig. 5(b)) is zero. In comparison, at $2f_0$, the generated common-mode signal is blocked by Slot2, because the cutoff frequency for the associated TM-mode wave is ~6 THz. Such mode-filtering mechanism effectively isolates the harmonic signal from the lossy transistor gates (Fig. 5(c)). Meanwhile, $2f_0$ Slot1 is half-wavelength, and works as an on-chip folded-slot antenna, because all the standing waves inside the folded branches are in-phase. Such compact, close-to-device radiator structure achieves 45% radiation efficiency in simulation.

Under the RX mode, the incident wave at $2f_0 \pm f_{IF}$ is coupled by the same reciprocal antenna Slot1. The MOSFETs now behave as a resistive-mode sub-harmonic mixer with the large-power input at f_0 as LO signal. The IF signal is extract from the top of AMP through an integrated RF choke (Fig. 5(a)) and an external bias tee. With signal filtering at the output, the down-converted irrelevant comb lines are not presented at base-band. For the entire comb spectrometer, 10 IF channels can be connected to separate external IF amplifiers and detectors for parallel data processing.

[1]For the detailed theoretical analysis and design of such feedback, please refer to [22] by the same authors.

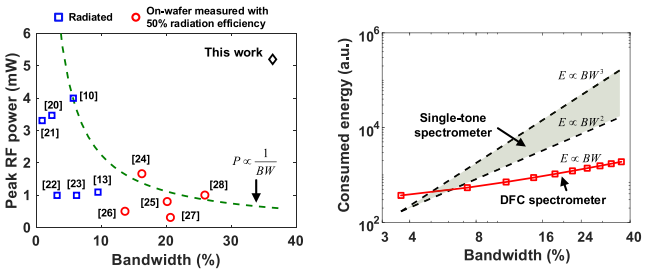

(a) (b)

Fig. 6. Advantages of the presented comb spectrometer: (a) comparison with other state-of-the-arts silicon circuits above 200 GHz in terms of radiated power versus bandwidth, and (b) the total energy consumption versus bandwidth.

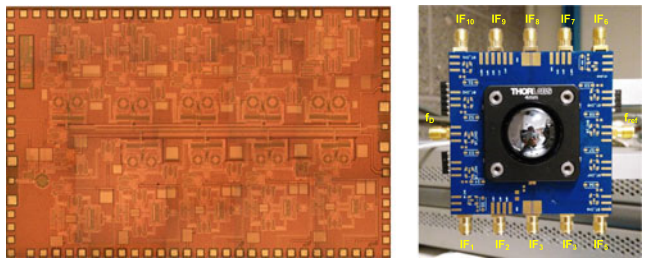

(a) (b)

Fig. 7. Photograph of: (a) CMOS THz comb transceiver based on 65-nm bulk CMOS process (2×3 mm^2) and (b) the packaged chip on PCB with 1-inch diameter silicon lens attached at the backside.

C. Advantages of Dual-Frequency-Comb Spectrometer

Compared to prior optical combs based on mode-locked laser pulse [27],[28], the CW-type electronic comb offers excellent tuning capability, phase coherency, and high frequency resolution. It also enables scalability to higher bandwidth through extended cascading of AMP channels. In the dual-frequency-comb architecture, since 10 probing comb pairs work simultaneously, it leads to a much faster scanning speed through parallel operation by at least a factor of 20×. In addition to that, significant spectroscopic performance is gained, due to the following reasons.

Firstly, our chip architecture breaks the bandwidth-efficiency tradeoff of conventional RF-to-THz designs, as mentioned in Section I. By partitioning the overall spectrum, the required tuning range for each channel is reduced below 4.5%, which allows for high-Q topology (e.g. the dual-transmission-line feedback in AMPs) and keeps peak performance across a broad frequency range. Shown in Fig. 6(a) is a statistic of silicon-based sources above 200 GHz, which exhibits clear inversely proportional dependency between the radiated power and bandwidth. In contrast, our work demonstrates broad bandwidth without degrading the radiated power and noise performance.

Secondly, as is discussed in Section II-D, the maximum radiated power, is limited by the saturation effect of molecules, especially for small-size gas cells. Subsequently, it determines the ultimate sensitivity for a given total scanning time. In our comb, the total radiated power exceeds such limitation while keeping each single tone still below the saturation threshold. Given an fixed total scanning time and total bandwidth, since the integration time per frequency point is 20× longer (i.e., smaller $\Delta\nu$ in (11)) due to the parallelism, the comb architecture achieves better sensitivity.

Thirdly, the energy efficiency is significantly improved. Due to the aforementioned bandwidth-efficiency tradeoff, the total energy consumption of conventional single-tone spectrometers has a square or cubic dependency over operational bandwidth (Fig. 6(b)). In comparison, without extending scanning time, the energy consumption of dual-frequency-comb spectrometer increases linearly with higher bandwidth (i.e., more cascading comb stages). The simultaneous transmit-receive scheme enabled by our AMP design further reduces the energy consumption by ∼2×. For an fractional bandwidth of ∼40% (this work), the estimated overall energy saving is 10 to 100× compared with conventional spectrometer scheme.

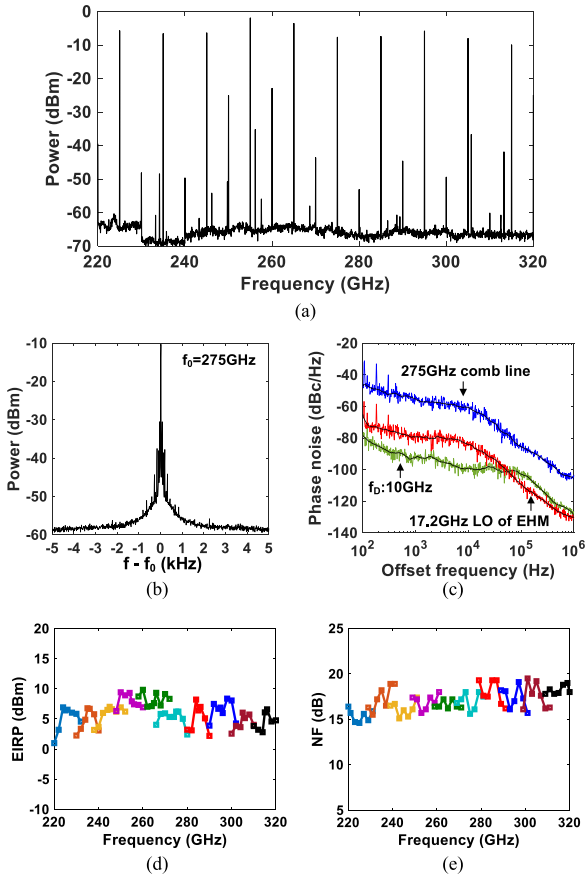

Fig. 8. Measurement results of (a) the spectrum of 10 comb lines from 225-to-315GHz with 10-GHz spacing, (b) the spectrum of 275-GHz comb line with 10-kHz span, (c) the phase noise of the 275-GHz comb line, 10-GHz reference signal and 17.2-GHz LO signal for EHM (16th harmonic) used for comb-line phase noise measurement, (d) effective isotropic radiated power (EIRP), and (e) single sideband noise figure (SSB NF).

IV. Experimental Results

The comb spectrometer chip is fabricated using TSMC 65-nm bulk CMOS process ($f_{\max} = 250$ GHz). The chip size is 3×2 mm^2 and the die photo is shown in Fig. 7(a). The chip is mounted on an FR-4 PCB with wire bonding. A 1-inch diameter high-resistivity silicon lens is attached to the backside of the chip

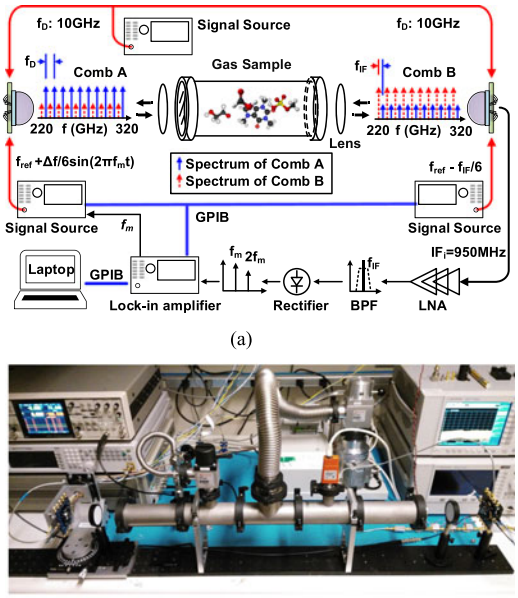

(a)

(b)

Fig. 9. (a) Schematic and (b) photograph of THz spectroscopy setup.

(shown in Fig. 7(b)), in order to enhance the radiation coupling to free space. The lens has a hemispheric shape, so the beam out of the chip is not further collimated.

A. Electrical Performance of the CMOS Chip

Fig. 8(a) presents the measured comb spectrum from 220 to 320 GHz using a horn-antenna-fed, even-harmonic mixer (from VDI Inc.) and a spectrum analyzer with a resolution bandwidth of 100 kHz. The undesired spurs in Fig. 8(a) result from the inter-modulation within the up- and down- conversion chains, and they are at least 20 dB lower than the comb lines. Fig. 8(b) presents the spectrum of 275-GHz comb line with 10-kHz span. The measured phase noise for the 275-GHz comb line is -102 dBc/Hz at 1-MHz offset as shown in Fig. 8(c). By tuning the input driving signal ($f_{\rm ref}$ in Fig. 4), the chip covers the 220-to-320 GHz bandwidth seamlessly. Using an Erickson PM-4 power meter, the effective isotropic radiated power (EIRP) of each comb line under TX mode ismeasured[2] and plotted in Fig. 8(d). The measured average radiation directivity of the AMPs is10.1 dBi. The total radiated power of the 10 comb lines reaches 5.2 mW. The measured EIRP exhibits a variation of 10 dB within 220 $\sim$320 GHz, which results from the limited diameter of silicon lens compared with the dimension of CMOS chip. Each on-chip antenna thus has a non-negligible offset to the geometric center of the lens, and generates radiation beam deviated towards slightly different direction. In the RX mode, the SSB noise figure (NF) of each AMP is measured by using an OML network analyzer frequency extender as the broadband radiation source. Shown in Fig. 8(e), the NF including the loss of the on-chip antennas, ranges from 14.6 to 19.5 dB within the operational bandwidth.

[2]During this measurement, the DC bias of other irrelevant AMPs is cut off.

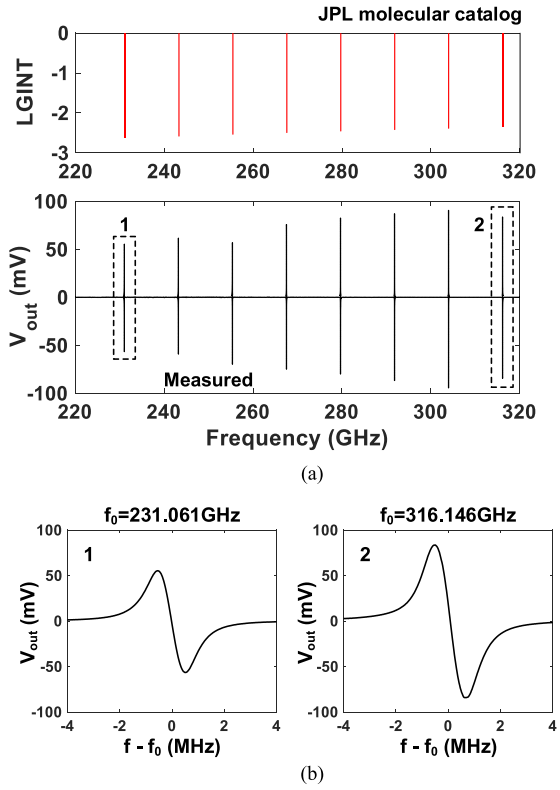

(a)

(b)

Fig. 10. Measured spectrum of OCS using WMS at f_m : (a) full band spectrum versus the recorded integrated intensity (LGINT) from JPL molecular catalog and (b) details of OCS spectral lines at 231.061 GHz and 316.146 GHz, respectively.

The DC power consumption of the chip is 1.7 W. The corresponding energy efficiency is 90 mJ/point with 1 Hz bandwidth or 0.5 s integration time in spectral sampling. The 10 AMPs consume a total DC power of 287 mW, which corresponds a DC-to-THz efficiency of 1.8%. 1.177 W of the total DC power is consumed by 41 inter-stage buffer amplifiers. The 9 up/down conversion mixers (including static frequency divider) consume 199 mW. The input tripler consumes 32 mW. The overall DC-to-THz efficiency is 0.3%.

B. Demonstration of THz Spectroscopy

A spectroscopy experimental setup is built as shown in Fig. 9(a). The demonstration system adopts free space radiation and a 70 cm gas cell with 2 inches diameter instead of the single-mode waveguide mentioned in Section II-E. The sample is injected from a gas cylinder with its pressure precisely controlled by a turbo molecular pump and a vacuum gauge. Two CMOS comb chips are used as transceivers, which are driven by two phase-synchronized signal sources (with a frequency difference to generate $f_{IF} = 950$ MHz). The output/input beams of the chips are collimated using a pair of Teflon lenses, and are coupled to the gas chamber through quartz vacuum windows. Wavelength modulation spectroscopy (WMS) with a modulation frequency f_m of 50 kHz and a frequency deviation Δf of 360 kHz is performed. A lock-in amplifier (Stanford Research

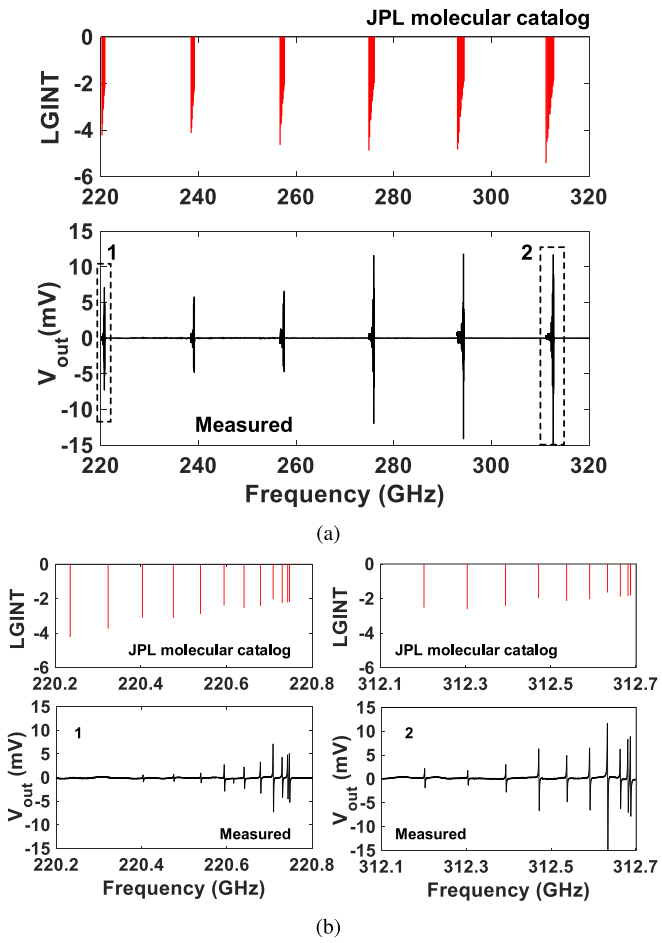

Fig. 11. Measured spectrum of CH_3CN using WMS at f_m versus the integrated intensity (LGINT) from JPL molecular catalog: (a) full band spectrum and (b) details of two spectral sections located at 220.2-to-220.8 GHz and 312.1-to-312.7 GHz, respectively.

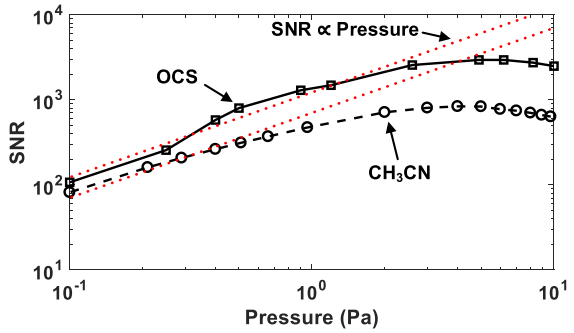

Fig. 12. $SNR_{v/v}$ variation versus pressure degradation for the 279.685 GHz spectral line of OCS and the 294.251 GHz spectral line of acetonitrile ($\Delta\nu =$ 78 Hz).

SR865A) generates the f_m modulation signal and measures the amplifier output envelope of the baseband rectifier, which contains the spectral information. Due to the limited hardware, the molecular spectrum is scanned channel by channel.

Firstly, based on the measured chip performance in Section IV-A, the link budget is calculated to estimate sensitivity. For a typical channel at 275 GHz ($\lambda = 1.1$ mm), if no lens

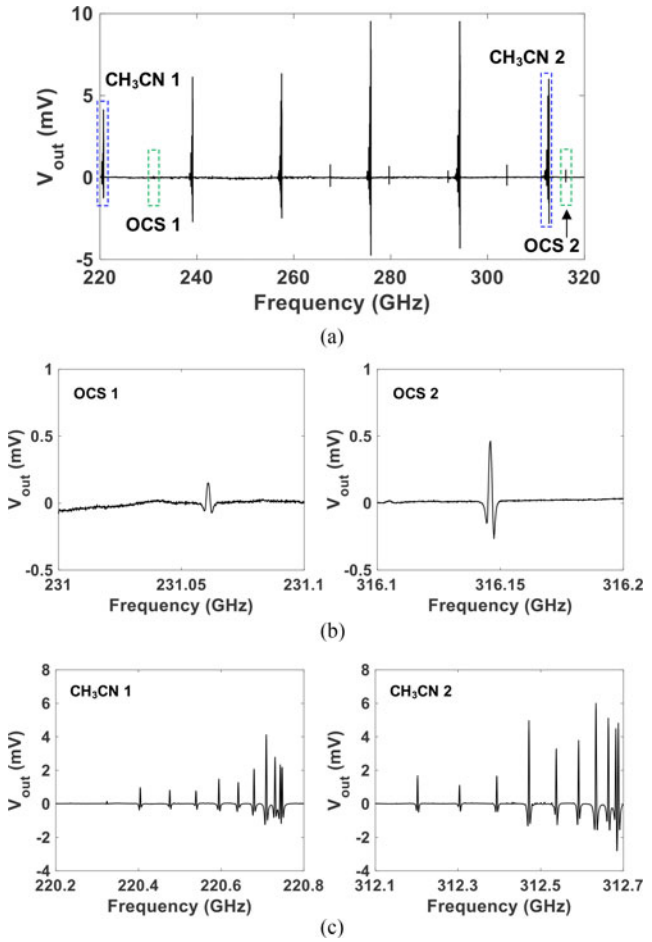

Fig. 13. Measured spectrum of CH_3CN and OCS gas mixture using WMS at $2f_m$: (a) full band spectrum. (b) details of 231.061 GHz and 316.146 GHz spectral lines of OCS in the mixture. (c) details of 220.2-to-220.8 GHz and 312.1-to-312.7 GHz spectral lines of CH_3CN in the mixture.

nor gas cell is placed, the link SNR can be estimated by:

$$SNR_{linkbudget} = \frac{P_0 D^2 \lambda^2}{(4\pi L)^2 k T_n} = 92\,\text{dB}\,(\Delta\nu = 1\,\text{Hz}), \quad (26)$$

where an emitted power P_0 of 0.5 mW, an SSB NF of 17 dB, a total path length L of 1 m and a typical directivity D of 10 dBi are used. When the loss from vacuum windows, gas cell and internal reflection is included, the SNR will be even lower. Fortunately, with the well-aligned Teflon lenses, which increase the link budget by ~20 dB, the actual SNR reaches 98 dB (1-Hz bandwidth) in our measurement. This indicates that our spectrometer has a minimum detectable absorption of $\alpha_{\text{gas,min}} = 7.2 \times 10^{-7}$ cm^{-1} according to (22). The maximum detectable absorption of the current system is 6.6×10^{-2} cm^{-1}, which corresponds to 99% absorption over a 70 cm path. Therefore, the dynamic range of the current system is 50 dB.

Next, spectroscopy for carbonyl sulfide (OCS) is investigated. Fig. 10(a) presents the measured spectrum of OCS from 220-to-320 GHz under 10-Pa pressure, which matches the JPL molecular catalog [12], and exhibits a period of 12.15 GHz. The entire spectrum is recorded by WMS at f_m with a 100-kHz frequency step. The integration bandwidth is 0.78 kHz.

TABLE II
PERFORMANCE COMPARISON OF ROTATIONAL SPECTROMETER

Ref.	Spectrometer Architecture	Technology	Frequency (GHz)	TX Radiated Power (mW)	RX SSB Noise Figure (dB)	Path Length (m)	Minimum Detectable Absorption (cm^{-1}) with 1-Hz bandwidth
[11]	Single-Tone	GaAs Schottky Barrier Diode	210 ~270	~1[1]	~14	1.2	2.7×10^{-9}[2]
[14]	Single-Tone	0.13 μm SiGe BiCMOS	238 ~252	5	18	1.9	4.3×10^{-6}[3]
[16]	Single-Tone	65 nm CMOS	208 ~255	0.1[4]	N/A	1	N/A
[19]	Pulsed Echo	65 nm CMOS	95 ~105	4	9.2	0.03[5]	N/A
This Work	Dual-Frequency-Comb	65 nm CMOS	220 ~320	5.2[6]	14.6 ~19.5	0.7	7.2×10^{-7}

[1] The radiated power and noise figure are estimated from performance of typical VDI instrument.
[2] $\alpha_{\text{gas,min}} \approx 0.017\ \text{cm}^{-1}/(500 \times \sqrt{1\ \text{s}/0.01\ \text{s}} \times 10\,\text{Pa}/0.008\,\text{Pa}) = 2.7 \times 10^{-9}\,\text{cm}^{-1}$ is calculated based on CH_3CN with pressure of 6×10^{-5} Torr (0.008 Pa). The reported SNR is 500 with 0.01 s integration time.
[3] $\alpha_{\text{gas,min}} \approx 0.0013\ \text{cm}^{-1}/300 = 4.3 \times 10^{-6}\ \text{cm}^{-1}$ is calculated based on 248.28 GHz spectral line of CH_3OH with pressure of 13 Pa. Its absorption coefficient is 0.0013 cm^{-1} based on [40]. The measured SNR is 300 based on Fig.18 of [14]. The integration time hasn't been specified.
[4] The reported power is EIRP, which includes the antenna gain of the chip.
[5] Effective path length is larger than physical length due to multi-reflection inside high Q semiconfocal cavity.
[6] Total radiated power of THz comb. The average radiated power is 0.5 mW for each comb line.

10 ms is required for each data point, which is mainly limited by the time response and communication of instruments. As a result, the measurement time for each channel with 10-GHz bandwidth is 10^3 seconds. In future applications where dual-frequency-comb scanning and custom-designed peripheral circuitry are adopted, only ~500 seconds (or ~8 minutes) should be needed for 100-GHz bandwidth with 10-kHz step size and 1-kHz integration bandwidth. Details of two OCS spectral lines at 231.061 GHz and 316.146 GHz are shown in Fig. 10(b). Their full width at half maximum (FWHM)[3] is ~1 MHz. According to [40], the peak absorption coefficient $\alpha_{OCS,pure}$ of the 279.685-GHz spectral line under 10-Pa pressure is 0.040 cm^{-1}, which leads to 94% absorption through the 70-cm-long gas chamber. According to (10), this corresponds to a baseband SNR of $(1 - 0.06^{0.5}) \times 0.5 \times 10^{98/20} = 3.0 \times 10^4$ (or 89.5 dB). In Fig. 10(a), the peak signal amplitude of 279.685-GHz spectral line is 83 mV and the measured baseband RMS noise voltage V_{noise} is 2.8 $\mu\text{V}/\sqrt{Hz}$; as a result, the output $\text{SNR}_{v/v}$ is 2.9×10^4 (or 89.2 dB) with 1 Hz bandwidth. We note that this matches the theoretical calculation of 3.0×10^4 very well, which further validates our analysis in Section II-A.

At the pressure of 10 Pa, the spectrum of another molecule, acetonitrile (CH_3CN), between 220 to 320 GHz with a period of 18.4 GHz is also measured and shown in Fig. 11(a). Details of two spectral sections within 220.2-to-220.8 GHz and 312.1-to-312.7 GHz are given in Fig. 11(b), which again agree with the JPL molecular catalog [12]. The peak absorption coefficient for the 294.251-GHz spectral line (at 10 Pa) is 0.017 cm^{-1}. An output baseband $\text{SNR}_{v/v}$ of 7.4×10^3 is measured for 1 Hz bandwidth. This is lower than the theoretical SNR derived from (11), mainly because the pressure-broadening effect for acetonitrile is more significant at 10 Pa, and the frequency deviation that we used ($\Delta f = 360$ kHz) does not optimally match the larger molecular linewidth (~2 MHz). As is seen next, such discrepancy does not exist when the pressure is reduced below the Doppler-limited threshold.

Fig. 12 shows the change of SNR under the reduction of sample pressure (i.e., molecule concentration) for the spectral line of OCS at 279.685 GHz and the spectral line of acetonitrile at 294.251 GHz. As predicted in (11), the $\text{SNR}_{v/v}$ scales linearly with the pressure when the pressure is sufficiently low. Based on the linear extrapolation, for OCS spectral line at 279.658 GHz, unity SNR under 1 Hz bandwidth is associated with a sample pressure of 1.1×10^{-4} Pa. This means, for a gas sample with 10-Pa pressure (i.e., no significant pressure broadening), an OCS concentration of 1.1×10^{-5} or 11 *ppm* is detectable. Similarly, for spectral line of acetonitrile at 294.251 GHz, the sensitivity under the same condition is $\times 10^{-5}$ or 14 ppm. According to Table I, if our setup is used to detect hydrogen cyanide (HCN), which has ~4× stronger absorption compared to OCS, the sensitivity should reach 3 *ppm*,[4] At present, sample pre-concentration technology is widely adopted in gas sensing, which can provide a concentration gain of 10^5. If our CMOS chipset is used in a setup with such pre-concentration, a sensitivity at 10 ~100-*ppt* level should be achievable.

Lastly, there is one possible error that the TX spurs shown in Fig. 8(a) probe the spectral lines, which are then subsequently down-converted into IF band by mixing with corresponding LO spurs in the RX. However, in simulation, the LO-power-dependent mixer conversion loss is 84 dB, and the resultant inter-modulation components in IF band are ~100 dB lower than the actual IF signals. Thus, it is not a limiting factor of the sensitivity. For validation, Fig. 13(a) presents the measured spectrum of an OCS and CH_3CN gas mixture. The pressure of the gas mixture is 10 Pascal. The volume ratio of the two gas samples is $V_{OCS} : V_{CH_3CN} \approx 1 : 60$. To further reduce the baseline ripple, WMS at $2f_m$ is performed. The measured spectra (shown in Fig. 13(b) and (c)) are examined; no false spurs are observed besides the superposed OCS and CH_3CN spectra.

[3]The FWHM of the spectral line is $1/\sqrt{3}$ of the peak-to-peak distance of the plot generated using wavelength modulation spectroscopy [39] (such as Fig. 10(b)), as is illustrated in Fig. 1(c).

[4]This is not experimentally validated, because HCN is highly toxic.

V. Conclusion

A CMOS dual-frequency-comb spectrometer is presented in this paper. A comparison between this work and previous publications is given in Table II. Through a parallel spectral scanning using 20 comb lines, this spectrometer achieves more than 20× speed enhancement and breaks the bandwidth-efficiency tradeoff in conventional circuit design. A total radiated power of 5.2 mW and a 14.6-to-19.5 dB SSB NF are obtained in measurements, which are not only the best among all silicon-based THz electronics, but also even comparable with the performance of compound semiconductor devices (e.g., GaAs Schottky-barrier diode). The measured minimum detectable absorption coefficient of this work is 7.2×10^{-7} cm^{-1}, which is higher than the prior work in silicon, but still two orders lower than that reported in [13]. This is mainly because of the lower on-chip antenna gain (10 dBi versus 25 dBi in [13] for TX and RX). Such problem can be solved in the future by implementing multiple coherent radiators for each comb channel (hence higher antenna gain).

In addition, fundamentals of frequency scanning spectrometer are discussed and validated. The measured SNR matches the theoretical prediction. The Townes noise due to square-law detection is the major limiting factor for sensitivity so far, which leads to a linear dependency of SNR versus gas concentration. It is an interesting issue to be addressed before we encounter shot noise. Based on the current silicon semiconductor technology, the sensitivity of a fully-optimized spectrometer should reach below 1-*ppm* level (or below 10-*ppt* with pre-concentration).

This technology is expected to be applied in future biomedical areas. The concentration of volatile organic compounds (VOCs) in human exhaled breath ranges from *ppm* to *ppb* level [1], [4], and the fluctuation of specified VOCs, normally at *ppb* level, can be utilized as bio-markers for disease diagnosis. As shown in this work, sufficient sensitivity is provided by silicon-based rotational spectrometers. This enables fast, non-invasive monitoring/analysis of human health conditions.

Acknowledgment

The authors would like to acknowledge Dr. S. Coy, Prof. R. Field, Prof. K. Nelson (Chemistry Department, MIT), Prof. J. Muenter (Chemistry Department, University of Rochester), and Prof. Q. Hu (EECS Department, MIT) for technical discussions. They appreciate Dr. R. Temkin (Physics Department, MIT), Prof. E. Afshari (EECS Department, University of Michigan), Prof. A. Chandrakasan, and Prof. T. Palacios (EECS Department, MIT) for their support of testing instruments. They also thank Y. Zhang (Chemistry Department, MIT) and T. Shi (Fudan University and MIT) for their technical assistances. The chip fabrication of this work was provided by TSMC University Shuttle Program.

References

[1] F. K. Tittel *et al.*, "Recent advances and applications of mid-infrared based trace gas sensor technology," *Proc. SPIE*, vol. 6900, 2008, Art. no. 69000Z.

[2] O. Varghese, "Exhaled gas detection for medical diagnosis: Can it be made a tool for self-screening," *J. Nanomed Res.*, vol. 3, no. 3, 2016, Art. no. 00056.

[3] I. R. Medvedev *et al.*, "Analysis of exhaled human breath via terahertz molecular spectroscopy," in *Proc. 2016 41st Int. Infrared, Millimeter, THz Waves Conf.*, 2016, pp. 1–2.

[4] I.-D. Kim, S.-J. Choi, S.-J. Kim, and J.-S. Jang, "Exhaled breath sensors," in *Smart Sensors for Health and Environment Monitoring*. New York, NY, USA: Springer, 2015, pp. 19–49.

[5] A. Amann *et al.*, "Analysis of exhaled breath for disease detection," *Annu. Rev. Analytical Chem.*, vol. 7, pp. 455–482, 2014.

[6] H. Günzler and H.-U. Gremlich, *IR Spectroscopy. An introduction*. Weinheim, Germany: Wiley-VCH, 2002.

[7] P. S. Waggoner and H. G. Craighead, "Micro-and nanomechanical sensors for environmental, chemical, and biological detection," *Lab Chip*, vol. 7, no. 10, pp. 1238–1255, 2007.

[8] Q. Wan *et al.*, "Fabrication and ethanol sensing characteristics of Zno nanowire gas sensors," *Appl. Phys. Lett.*, vol. 84, no. 18, pp. 3654–3656, 2004.

[9] W. Pang, H. Zhao, E. S. Kim, H. Zhang, H. Yu, and X. Hu, "Piezoelectric microelectromechanical resonant sensors for chemical and biological detection," *Lab Chip*, vol. 12, no. 1, pp. 29–44, 2012.

[10] C. H. Townes and A. L. Schawlow, *Microwave Spectroscopy*. North Chelmsford, MA, USA: Courier Corporation, 2013.

[11] I. R. Medvedev, C. F. Neese, G. M. Plummer, and F. C. De Lucia, "Submillimeter spectroscopy for chemical analysis with absolute specificity," *Opt. Lett.*, vol. 35, no. 10, pp. 1533–1535, 2010.

[12] Jet Propulsion Laboratory, "Molecular Spectroscopy Catalog," 2018. [Online]. Available: https://spec.jpl.nasa.gov/

[13] C. F. Neese, I. R. Medvedev, G. M. Plummer, A. J. Frank, C. D. Ball, and F. C. De Lucia, "Compact submillimeter/terahertz gas sensor with efficient gas collection, preconcentration, and ppt sensitivity," *IEEE Sensors J.*, vol. 12, no. 8, pp. 2565–2574, Aug. 2012.

[14] K. Schmalz *et al.*, "245-GHz transmitter array in SiGe BiCMOS for gas spectroscopy," *IEEE Trans. THz Sci. Technol.*, vol. 6, no. 2, pp. 318–327, Mar. 2016.

[15] K. Schmalz, N. Rothbart, P. F.-X. Neumaier, J. Borngräber, H.-W. Hübers, and D. Kissinger, "Gas spectroscopy system for breath analysis at mm-wave/THz using SiGe BiCMOS circuits," *IEEE Trans. Microw. Theory Techn.*, vol. 65, no. 5, pp. 1807–1818, May 2017.

[16] N. Sharma *et al.*, "200–280 GHz CMOS RF front-end of transmitter for rotational spectroscopy," in *Proc. 2016 IEEE Symp. VLSI Technol.*, 2016, pp. 1–2.

[17] D. J. Nemchick, B. J. Drouin, A. J. Tang, Y. Kim, and M. C. F. Chang, "Sub-doppler spectroscopy with a CMOS transmitter," *IEEE Trans. THz Sci. Technol.*, vol. 8, no. 1, pp. 121–126, Jan. 2018.

[18] R. Han and E. Afshari, "A CMOS high-power broadband 260-GHz radiator array for spectroscopy," *IEEE J. Solid-State Circuits*, vol. 48, no. 2, pp. 3090–3104, Dec. 2013.

[19] A. Tang, B. Drouin, Y. Kim, G. Virbila, and M.-C. F. Chang, "95 105 GHz 352 MW all-silicon cavity-coupled pulsed echo rotational spectroscopy system in 65 nm CMOS," *IEEE Trans. THz Sci. Technol.*, vol. 7, no. 3, pp. 244–249, May 2017.

[20] Y. D. Hsieh *et al.*, "Terahertz comb spectroscopy traceable to microwave frequency standard," *IEEE Trans. THz Sci. Technol.*, vol. 3, no. 3, pp. 322–330, May 2013.

[21] C. Wang and R. Han, "Rapid and energy-efficient molecular sensing using dual mm-wave combs in 65 nm CMOS: A 220-to-320 GHz spectrometer with 5.2 mW radiated power and 14.6-to-19.5 dB noise figure," in *Proc. Int. Solid-State Circuit Conf.*, San Francisco, CA, USA, 2017, pp. 18–20.

[22] C. Wang and R. Han, "Dual-terahertz-comb spectrometer on CMOS for rapid, wide-range gas detection with absolute specificity," *IEEE J. Solid-State Circuits*, vol. 52, no. 12, pp. 3361–3372, Dec. 2017.

[23] J. M. Supplee, E. A. Whittaker, and W. Lenth, "Theoretical description of frequency modulation and wavelength modulation spectroscopy," *Appl. Opt.*, vol. 33, no. 27, pp. 6294–6302, 1994.

[24] J. Rogers, C. Plett, and F. Dai, *Integrated Circuit Design for High-speed Frequency Synthesis*. Norwood, MA, USA: Artech House, 2006.

[25] J. H. Van Vleck and V. F. Weisskopf, "On the shape of collision-broadened lines," *Rev. Modern Phys.*, vol. 17, no. 2/3, pp. 227–236, 1945.

[26] R. Spence, *Linear Active Networks*. New York, NY, USA: Wiley-Interscience, 1970.

[27] Y.-D. Hsieh *et al.*, "Terahertz comb spectroscopy traceable to microwave frequency standard," *IEEE Trans. THz Sci. Technol.*, vol. 3, no. 3, pp. 322–330, May 2013.

[28] D. Burghoff *et al.*, "Terahertz laser frequency combs," *Nature Photon.*, vol. 8, no. 6, pp. 462–467, 2014.

[29] S. Jameson, E. Halpern, and E. Socher, "20.4 a 300 Ghz wirelessly locked 2 × 3 array radiating 5.4 dBm with 5.1% DC-to-RF efficiency in 65 nm CMOS," in *Proc. 2016 IEEE Int. Solid-State Circuits Conf.*, 2016, pp. 348–349.
[30] R. Han *et al.*, "25.5 a 320 GHz phase-locked transmitter with 3.3 MW radiated power and 22.5 dBm EIRP for heterodyne THz imaging systems," in *Proc. 2015 IEEE Int. Solid-State Circuits Conf.*, 2015, pp. 1–3.
[31] U. R. Pfeiffer *et al.*, "14.5 a 0.53 THz reconfigurable source array with up to 1 MW radiated power for terahertz imaging applications in 0.13 μm SiGe BiCMOS," in *Proc. IEEE Int. Solid-State Circuits Conf. Digest Tech. Papers*, 2014, pp. 256–257.
[32] X. D. Deng, Y. Li, J. Li, C. Liu, W. Wu, and Y. Z. Xiong, "A 320-GHz 1 × 4 fully integrated phased array transmitter using 0.13-μm SiGe BiCMOS technology," *IEEE Trans. THz Sci. Technol.*, vol. 5, no. 6, pp. 930–940, Nov. 2015.
[33] G. Liu, J. Jayamon, J. Buckwalter, and P. Asbeck, "Frequency doublers with 10.2/5.2 dBm peak power at 100/202 GHz in 45 nm SOI CMOS," in *Proc. Radio Freq. Integr. Circuits Symp.*, 2015, pp. 271–274.
[34] H.-C. Lin and G. M. Rebeiz, "A 200-245 GHz balanced frequency doubler with peak output power of +2 dBm," in *Proc. Compound Semicond. Integr. Circuit Symp.*, 2013, pp. 1–4.
[35] B. Cetinoneri, Y. A. Atesal, A. Fung, and G. M. Rebeiz, "W-band amplifiers with 6-dB noise figure and milliwatt-level 170–200-Ghz doublers in 45-nm CMOS," *IEEE Trans. Microw. Theory Techn.*, vol. 60, no. 3, pp. 692–701, Mar. 2012.
[36] R. Kananizadeh and O. Momeni, "2.6 a 190.5 GHz mode-switching VCO with 20.7% continuous tuning range and maximum power of −2.1 dBm in 0.13 μm BiCMOS," in *Proc. IEEE Int. Solid-State Circuits Conf.*, 2016, pp. 46–47.
[37] N. Sharma, W. Choi, and K. Kenneth, "160–310 GHz frequency doubler in 65-nm CMOS with 3-dBm peak output power for rotational spectroscopy," in *Proc. IEEE Radio Freq. Integr. Circuits Symp.*, 2016, pp. 186–189.
[38] T. Chi, M.-Y. Huang, S. Li, and H. Wang, "17.7 a packaged 90-to-300 GHz transmitter and 115-to-325 GHz coherent receiver in CMOS for full-band continuous-wave mm-wave hyperspectral imaging," in *Proc. IEEE Int. Solid-State Circuits Conf.*, 2017, pp. 304–305.
[39] J. Vanier and L.-G. Bernier, "On the signal-to-noise ratio and short-term stability of passive rubidium frequency standards," *IEEE Trans. Instrum. Meas.*, vol. 1001, no. 4, pp. 277–282, Dec. 1981.
[40] I. GATS, "Spectral Calculator," 2018. [Online]. Available: http://www.spectralcalc.com

Cheng Wang received the B.E. degree in engineering physics from Tsinghua University, Beijing, China, in 2008 and the M.Sc. degree in radio physics from China Academy of Engineering Physics, Mianyang, China, in 2011. He is currently working toward the Ph.D. degree at the Department of Electrical Engineering and Computer Science, Massachusetts Institute of Technology, Cambridge, MA, USA. He joined the Institute of Electronic Engineering, Mianyang, China, as an Assistant Research Fellow from 2011 to 2015.

In 2016, he received the Analog Device, Inc., Outstanding Student Designer Award. In 2017, he received the IEEE Microwave Theory and Techniques Society Boston Chapter Scholarship. His research covers topics of millimeter/terahertz-wave gas spectroscopy, high-precision clock generation, broadband communication, and radar imaging.

Bradford Perkins received the B.A. degree in chemistry from Dartmouth College, Hanover, NH, USA, in 2001 and the Ph.D. degree in chemical physics from Joint Institute for Laboratory Astrophysics, University of Colorado, Boulder, CO, USA, in 2009 for studies that investigated dynamics at the gas-liquid interface. He was awarded a National Science Foundation Postdoctoral Fellowship in 2010 to work in the Chemistry Department, Massachusetts Institute of Technology, where he studied ultrafast processes in crystals and superconductors with THz spectroscopy.

Dr. Perkins is currently Technical Staff member in the Chemical, Microsystems, and Nanoscale Technologies Group, MIT Lincoln Laboratory, Lexington, MA, USA. His current research interests involve chemical and biological material sensing, aerosol chemistry, and novel laser-based spectroscopic techniques.

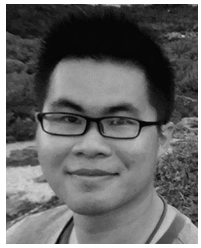

Zihan Wang is current working toward the B.Sc. degree at Chemistry Department, Fudan University, Shanghai, China. He was a visiting student in Massachusetts Institute of Technology, Cambridge, MA, USA, from May 9th, 2017 to August 21st, 2017. His research interest includes chemistry spectroscopy and nanomaterial synthesis.

Ruonan Han (S'10–M'14) received the B.Sc. degree in microelectronics from Fudan University, Shanghai, China, in 2007, the M.Sc. degree in electrical engineering from the University of Florida, Gainesville, FL, USA, in 2009, and the Ph.D. degree in electrical and computer engineering from Cornell University, Ithaca, NY, USA, in 2014. In 2012, he was an Intern with Rambus Inc., Sunnyvale, CA, USA, designing energy-efficient I/O circuits. He is currently an Assistant Professor with the Department of Electrical Engineering and Computer Science, Massachusetts Institute of Technology, Cambridge, MA, USA. His current research interests include microelectronic circuits and systems operating at millimeter-wave and terahertz frequencies for novel sensing and ultrahigh-speed communications.

Dr. Han is a member of the IEEE Solid-State Circuits Society and the IEEE Microwave Theory and Techniques Society. He was a recipient of the Cornell ECE Directors Ph.D. Thesis Research Award, the Cornell ECE Innovation Award, and two Best Student Paper Awards of the IEEE Radio-Frequency Integrated Circuits Symposium (2012 and 2017). He was also a recipient of the Irwin and Joan Jacobs Fellowship, the John M. Olin Fellowship, the IEEE Microwave Theory and Technique Society Graduate Fellowship Award, and the IEEE Solid-State Circuits Society Predoctoral Achievement Award. He currently holds MIT E. E. Landsman (1958) Career Development Chair Professorship, and is the winner of the National Science Foundation CAREER Award in 2017.